

# Bismuth Oxyhydroxide-Pt Inverse Interface for Enhanced Methanol Electrooxidation Performance

Xuchun Wang,<sup>§</sup> Miao Xie,<sup>§</sup> Fenglei Lyu,<sup>\*</sup> Yun-Mui Yiu, Zhiqiang Wang, Jiatang Chen, Lo-Yueh Chang, Yujian Xia, Qixuan Zhong, Mingyu Chu, Hao Yang, Tao Cheng,<sup>\*</sup> Tsun-Kong Sham,<sup>\*</sup> and Qiao Zhang<sup>\*</sup>



Cite This: *Nano Lett.* 2020, 20, 7751–7759



Read Online

ACCESS |

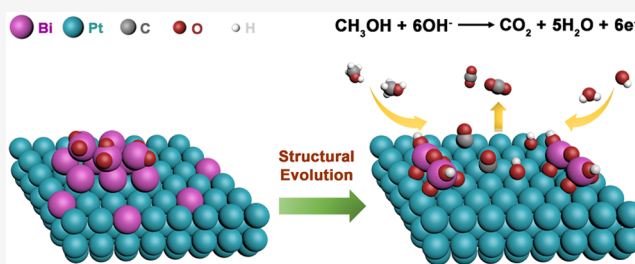
Metrics & More

Article Recommendations

Supporting Information

**ABSTRACT:** Developing efficient Pt-based electrocatalysts for the methanol oxidation reaction (MOR) is of pivotal importance for large-scale application of direct methanol fuel cells (DMFCs), but Pt suffers from severe deactivation brought by the carbonaceous intermediates such as CO. Here, we demonstrate the formation of a bismuth oxyhydroxide ( $\text{BiO}_x(\text{OH})_y$ )-Pt inverse interface via electrochemical reconstruction for enhanced methanol oxidation. By combining density functional theory calculations, X-ray absorption spectroscopy, ambient pressure X-ray photoelectron spectroscopy, and electrochemical characterizations, we reveal that the  $\text{BiO}_x(\text{OH})_y$ -Pt inverse interface can induce the electron deficiency of neighboring Pt; this would result in weakened CO adsorption and strengthened OH adsorption, thereby facilitating the removal of the poisonous intermediates and ensuring the high activity and good stability of  $\text{Pt}_2\text{Bi}$  sample. This work provides a comprehensive understanding of the inverse interface structure and deep insight into the active sites for MOR, offering great opportunities for rational fabrication of efficient electrocatalysts for DMFCs.

**KEYWORDS:** electrochemical reconstruction, inverse interface, methanol oxidation,  $\text{PtBi}$ , X-ray absorption spectroscopy



## INTRODUCTION

Direct methanol fuel cells (DMFCs) have emerged as one of the most promising power sources for portable devices and vehicles because of their unique advantages including high energy density, low operation temperature, and environmental benignancy.<sup>1–4</sup> The wide application of DMFCs has been seriously hindered by the low efficiency of the anode reaction, namely, the methanol oxidation reaction, because of its sluggish kinetics. Although Pt has been widely used as an electrocatalyst for MOR, it has suffered from several severe problems including its scarcity, high cost, and poor operation durability.<sup>5–8</sup> The low efficiency can be mainly ascribed to the susceptible nature of Pt to poisonous MOR intermediates, especially CO. How to boost the intrinsic activity of Pt and alleviate the adsorption of poisonous CO species on Pt are thereby crucial for developing highly efficient and durable Pt-based MOR electrocatalysts.<sup>5,9–12</sup>

To enhance the antipoisoning ability of Pt-based catalysts, one strategy is via alloying Pt with other metals, such as Ru,<sup>13,14</sup> Cu,<sup>15,16</sup> Ni,<sup>17–21</sup> and Co,<sup>22</sup> to tune the electronic structure of Pt, which thus weakens CO adsorption. In addition to the alloy system, some metal oxides<sup>23,24</sup> and hydroxides/oxyhydroxides<sup>25</sup> have been used to support Pt as they can facilitate the generation of abundant OH species for oxidative removal of adsorbed CO. Notably, the interface between Pt and the support plays a crucial role in improving

the catalytic performance since it provides the channel for charge redistribution and vicinity for intermediate spillover. Therefore, engineering the interface structure is beneficial to rational design of highly efficient catalysts. In recent years, inverse heterogeneous nanostructures, in which oxides or other compounds were decorated on the noble metal surface, have opened an avenue for construction of interface structure.<sup>26–29</sup> Heterogeneous catalysts with an inverse interface structure, particularly oxide/metal interface structure, have shown extraordinary catalytic performance in water–gas shift,<sup>30,31</sup> water splitting,<sup>32,33</sup> and CO oxidation,<sup>34,35</sup> mainly attributed to enhanced dissociation of water or oxygen at interfacial sites. However, the inverse interface has been seldom studied in MOR, although it provides a well-suitable structural model for investigating the synergistic effect between metal oxides and noble metals.

Besides, how to construct the inverse interface structure also faces challenges to its prevailing in electrocatalysis. Traditional bottom-up and top-down synthesis strategies are difficult to

Received: August 16, 2020

Revised: September 15, 2020

Published: September 22, 2020



directly tune the subtle interface structure considering multiple variable synthesis parameters. Recently, electrochemical treatment-induced structural evolution of electrocatalysts has played a great role in optimizing catalyst structure to improve their efficiency in an electrocatalytic system.<sup>36–38</sup> For example, Strasser and co-workers realized experimental control over the extent of dealloying (thickness of Pt-rich shell) in Pt–Cu nanoparticles through cyclic voltammetry scans, which could tune the lattice strain of the Pt-rich shell and weaken chemisorption of oxygenated species in oxygen reduction reaction (ORR).<sup>39</sup> Liao et al. tuned the areal ratio of the water dissociation component to the noble metal surface on a nano-Pd surface through an electrochemical cycling strategy, thereby effectively balancing the water dissociation step and the hydrogen formation step in the hydrogen evolution reaction (HER).<sup>32</sup> Given the structural variability of electrocatalysts at a reductive or oxidative potential, it would be a promising strategy to construct the inverse interface, underlying the mechanism study of inverse catalysts in MOR.

Over the past few years, bismuth as a cheap and efficient promoter has been widely incorporated in Pt-based electrocatalysts.<sup>40–43</sup> Bismuth oxide/hydroxide, particularly in the alcohol oxidation reaction, has been inextricably linked to generating OH species for oxidative removal of adsorbed CO, whereas deep insight into the synergy between Pt and Bi remains vague.<sup>44,45</sup> Herein, with the help of density functional theory (DFT) calculations, we reveal that the  $\text{BiO}_x(\text{OH})_y\text{-Pt}$  inverse interface can increase the positive charge on its neighboring Pt atoms, resulting in weakened CO adsorption and strengthened OH adsorption. Under the theoretical guideline, we have successfully synthesized PtBi catalysts with this kind of inverse interface structure through electrochemical reconstruction. A comprehensive depiction of the inverse interface structure in terms of geometric and electronic features is provided by combining X-ray absorption spectroscopy (XAS), ambient pressure X-ray photoelectron spectroscopy (AP-XPS), and electrochemical characterizations. The optimal  $\text{Pt}_2\text{Bi}$  sample manifests a high mass activity of  $4611 \text{ mA mg}^{-1}_{\text{Pt}}$ , which is 5.96 times higher than that of commercial Pt/C. Moreover, the  $\text{Pt}_2\text{Bi}$  sample can maintain a mass activity of  $1520 \text{ mA mg}^{-1}_{\text{Pt}}$  after a chronoamperometric test for 10000 s, which is much higher than that of Pt/C ( $278 \text{ mA mg}^{-1}_{\text{Pt}}$ ). This work highlights comprehensive understanding of the inverse interface structure and its electronic effect on Pt sites, shedding light on the rational design of highly efficient electrocatalysts.

## RESULTS AND DISCUSSION

In order to investigate the impact of the inverse interface on the catalyst surface, DFT calculations were performed based on two structural models, the Pt (111) surface and the Pt (111) surface with  $\text{BiO}_x(\text{OH})_y$ . For Pt decorated with  $\text{BiO}_x(\text{OH})_y$ , Pt (111) with three atomic layers in the bulk and two isolated  $\text{BiO}_x(\text{OH})_y$  on its surface was employed. During the geometry optimizations, two layers of atoms in the bottom were fixed at their bulk positions, whereas the rest of the atoms were allowed to relax (additional details about the simulation model and simulation methods are presented in the Supporting Information). Both O and Bi strongly bind on the interface as indicated from the short Pt–O and Pt–Bi distances, and the optimized composite interface is shown in Figure S1. Since the adsorption behavior of adsorbates is closely related to the electron status of the surface atoms, the Bader net charge of

surface atoms relating to adsorbates was calculated. The results show that Pt atoms on the surface of the  $\text{BiO}_x(\text{OH})_y\text{-Pt}$  system are more positively charged (electron deficient) compared to that of a pure Pt system (Table S1). The variation in Bader net charge is expected to tune the adsorption behavior of MOR intermediates, such as CO and OH species, whose binding energies are widely used descriptors for evaluating the MOR performance.<sup>46</sup> Therefore, the binding free energies of CO and OH species were calculated (Figure 1, Figure S2, and Table

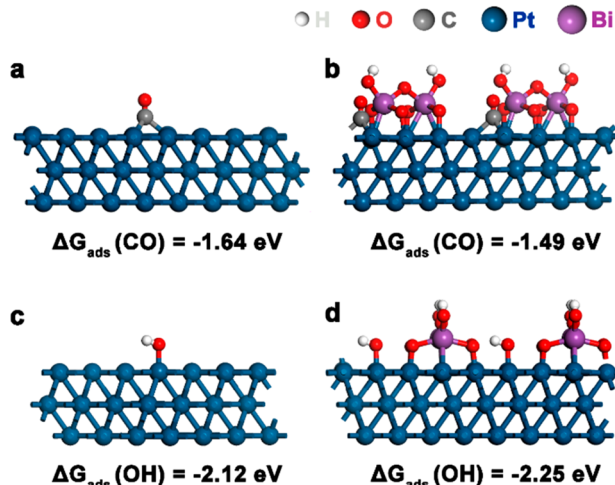


**Figure 1.** DFT calculation of the binding free energy of CO and OH species on surfaces of pristine Pt (111) (a and c) and Pt (111) with  $\text{BiO}_x(\text{OH})_y$  (b and d).

S2). The binding free energies of CO ( $\Delta G_{\text{ads}}(\text{CO})$ ) and OH ( $\Delta G_{\text{ads}}(\text{OH})$ ) on the Pt (111) surface are  $-1.64 \text{ eV}$  and  $-2.12 \text{ eV}$ , respectively. In contrast,  $\Delta G_{\text{ads}}(\text{CO})$  increases to  $-1.49 \text{ eV}$  and  $\Delta G_{\text{ads}}(\text{OH})$  decreases to  $-2.25 \text{ eV}$  at neighboring Pt atoms along with  $\text{BiO}_x(\text{OH})_y$ , indicating that the CO adsorption is weakened while OH adsorption is strengthened. The origination of adsorption behavior change should derive from the electron deficiency of Pt, which undermines the back-donation of electrons from the Pt 5d orbital to the empty  $2\pi$  orbital of CO, thereby weakening the bond between Pt and CO.<sup>47</sup> Conversely, the strongly electronegative O atoms in OH species prefer to form a strong interaction with electron-deficient Pt, contributing to the enhanced OH adsorption. To sum up, the electron deficiency of Pt brought by  $\text{BiO}_x(\text{OH})_y$  is proposed to weaken the CO adsorption and strengthen OH adsorption, which is expected to enhance CO tolerance and improve the activity and durability for MOR.

Inspired by DFT calculations, PtBi nanochains with a  $\text{BiO}_x(\text{OH})_y\text{-Pt}$  interface were delicately prepared through electrochemical reconstruction. In a typical synthesis, PtBi nanoparticles with controllable Pt/Bi ratios were synthesized through a polyol reduction method, in which chloroplatinic acid hexahydrate, bismuth neodecanoate, polyvinylpyrrolidone, and diethylene glycol were used as the metal precursors, surfactant, and solvent, respectively. The as-prepared products were then subjected to a chronoamperometric treatment for different times at  $-0.23 \text{ V}$  versus a saturated calomel electrode (SCE) to achieve the structural evolution in which treatment time was dependent on the Pt/Bi ratios. To confirm the formation of the proposed inverse interface structure,  $\text{Pt}_2\text{Bi}$  was taken as an example. The subscript indicates the feeding molar ratio of Pt/Bi precursors. Samples before and after

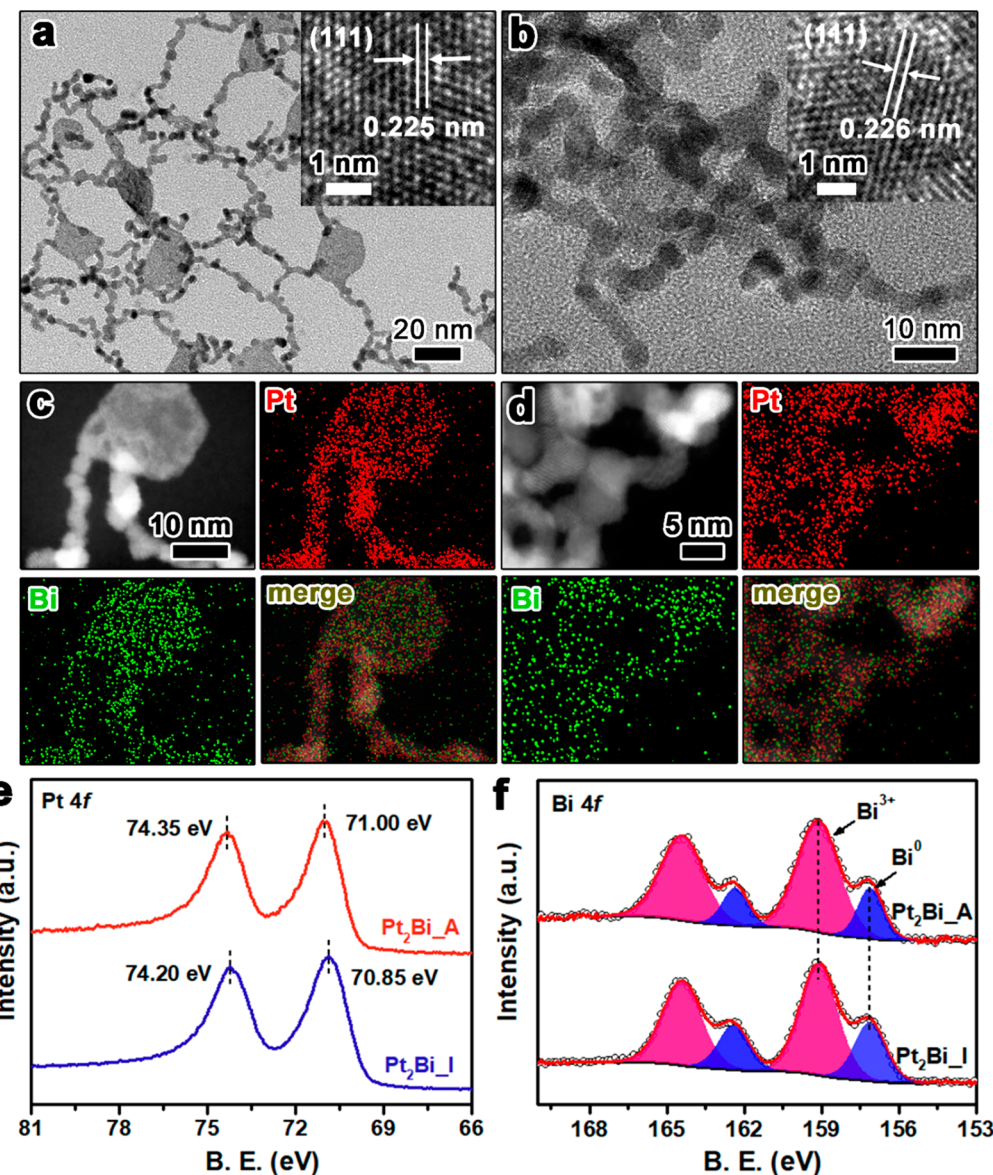


**Figure 2.** TEM images and HRTEM images of (a) Pt<sub>2</sub>Bi\_I and (b) Pt<sub>2</sub>Bi\_A. HAADF-STEM images and elemental mapping of (c) Pt<sub>2</sub>Bi\_I and (d) Pt<sub>2</sub>Bi\_A. XPS spectra of Pt<sub>2</sub>Bi\_I and Pt<sub>2</sub>Bi\_A at (e) Pt 4f and (f) Bi 4f orbitals.

electrochemical treatment are noted as Pt<sub>2</sub>Bi\_I and Pt<sub>2</sub>Bi\_A, respectively. The structural evolution was first monitored by TEM. Pt<sub>2</sub>Bi\_I consists of chain-like structures with an average diameter of 4.0 nm and plate-like structures with an average diameter of 20 nm (Figures 2a and S3). The lattice spacing of Pt<sub>2</sub>Bi\_I is measured to be about 0.225 nm (inset of Figure 2a), which can be indexed to the (111) facet of face-centered-cubic (fcc) Pt. The formation process of Pt<sub>2</sub>Bi\_I was monitored by characterizing the product at different times using TEM and EDS (Figures S4 and S5). Pt-rich short chains with a 4.0 nm diameter are formed at the initial stage and then attach to each other, generating chain-like structures. At 3 min, nanoplates appear and become larger afterward. No obvious morphology or composition change is observed after 30 min. After electrochemical treatment, Pt<sub>2</sub>Bi\_A maintains its chain-like structures while the nanoplates disappear (Figure 2b). Figure 2c shows the elemental distribution of Pt<sub>2</sub>Bi\_I, in which Pt and Bi elements disperse among all the particle regions and the average Pt/Bi atomic ratio is around 83.8:16.2 (Figure S6a).

Chains and plates possess different compositions, and the Pt/Bi ratio is 89.3:10.7 in chains while it is 56.8:43.2 in plates. Figure 2d shows a uniform elemental distribution after electrochemical treatment with a Pt/Bi ratio of 85.6:14.4 (Figure S6a). A slight increase in Pt/Bi ratio is ascribed to Bi leaching out mainly from plates during the electrochemical treatment, which also gives a possible explanation for the disappearance of plates. The crystal phase of Pt<sub>2</sub>Bi\_I and Pt<sub>2</sub>Bi\_A was characterized by X-ray diffraction (XRD), in which diffraction peaks at  $2\theta = 39.7^\circ, 46.3^\circ, 67.3^\circ, 81.5^\circ$ , and  $85.9^\circ$  are indexed as facets of fcc Pt (Figure S6b). Two additional peaks at  $2\theta = 26.5^\circ$  and  $54.8^\circ$  for Pt<sub>2</sub>Bi\_A are assigned to carbon paper which is used as a conductive support for collecting XRD sample.

In order to obtain a deeper understanding of the surface chemistry of Pt<sub>2</sub>Bi, X-ray photoelectron spectroscopy (XPS) was used to track changes in the electronic structure of Pt<sub>2</sub>Bi\_I and Pt<sub>2</sub>Bi\_A. For Pt<sub>2</sub>Bi\_I, two peaks at 70.85 and 74.20 eV are assigned to 4f<sub>7/2</sub> and 4f<sub>5/2</sub> orbitals of metallic Pt, respectively

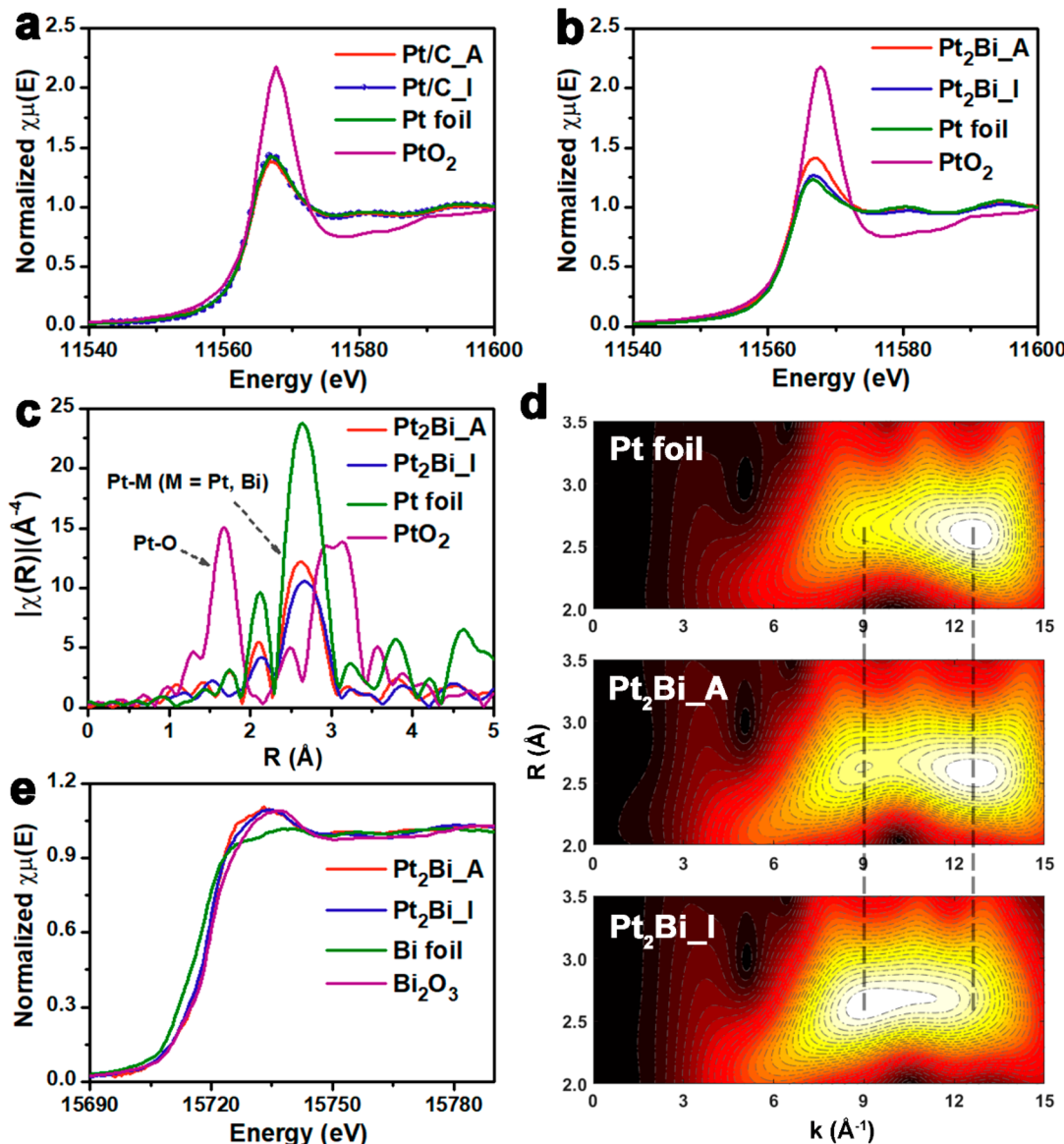


**Figure 3.** XANES spectra of (a) Pt/C and (b) Pt<sub>2</sub>Bi\_A before and after electrochemical treatment at the Pt  $L_3$ -edge. Pt foil and PtO<sub>2</sub> are used as references. Fourier transform (c) and wavelet transform (d) of the Pt  $L_3$ -edge EXAFS of Pt<sub>2</sub>Bi\_I and Pt<sub>2</sub>Bi\_A with a  $k^3$  weighting. Pt foil and PtO<sub>2</sub> are used as references. (e) XANES spectra of Pt<sub>2</sub>Bi\_I and Pt<sub>2</sub>Bi\_A at the Bi  $L_2$ -edge. Bi foil and Bi<sub>2</sub>O<sub>3</sub> are used as references.

(Figure 2e). Pt 4f orbitals of Pt<sub>2</sub>Bi\_A shift to a higher binding energy by 0.15 eV compared to that of Pt<sub>2</sub>Bi\_I, suggesting a higher oxidation state of Pt after electrochemical treatment. Figure 2f shows two sets of peaks of Bi 4f orbitals, in which peaks at 157.14 and 162.46 eV are assigned to  $4f_{7/2}$  and  $4f_{5/2}$  orbitals of metallic Bi while peaks at 159.12 and 164.42 eV are corresponding to  $4f_{7/2}$  and  $4f_{5/2}$  orbitals of Bi<sup>3+</sup> species. Although no obvious peak shift is observed at the Bi 4f orbitals, there is a noticeable decrease in metallic Bi after electrochemical treatment, which is confirmed by the decreasing integrated area ratio of Bi<sup>0</sup>/Bi<sup>3+</sup> from 0.43 to 0.28. The changes in oxidation state of Pt and Bi should be driven by anodic electrochemical oxidation. Moreover, the O 1s spectrum of Pt<sub>2</sub>Bi\_A shows an extra peak at a higher binding energy compared to that of Pt<sub>2</sub>Bi\_I (Figure S7), which can be assigned to metal–OH (M–OH), suggesting that Bi<sup>3+</sup> is mainly in the form of BiO<sub>x</sub>(OH)<sub>y</sub>.<sup>48</sup>

X-ray absorption spectroscopy (XAS) was further conducted to obtain the local electronic structure and coordination

environment. X-ray absorption near edge structure (XANES) and extended X-ray absorption fine structure (EXAFS) spectra were collected at the Pt  $L_3$ -edge and Bi  $L_2$ -edge. Commercial 20 wt % Pt/C catalyst was used for comparison. Figure 3a shows that the XANES spectra of commercial Pt/C before and after same electrochemical treatment at the Pt  $L_3$ -edge both overlap with that of Pt foil, indicating that Pt/C possesses the same local structure with Pt foil. The overlapping XANES spectra provide direct evidence for the absence of structure changes in Pt/C before and after electrochemical treatment. However, in the case of Pt<sub>2</sub>Bi catalyst, the whiteline intensity of Pt<sub>2</sub>Bi\_I catalyst is slightly higher than that of Pt foil while a noticeable enhancement is observed after electrochemical treatment (Figure 3b). The enhanced whiteline intensity indicates more unoccupied valence states at Pt sites (less electrons in the Pt 5d orbital), keeping in line with XPS results and the DFT calculation. The enhanced whiteline also can be observed in Pt<sub>4</sub>Bi and PtBi after electrochemical treatment (Figure S8). Fourier transform (phase-uncorrected) of EXAFS

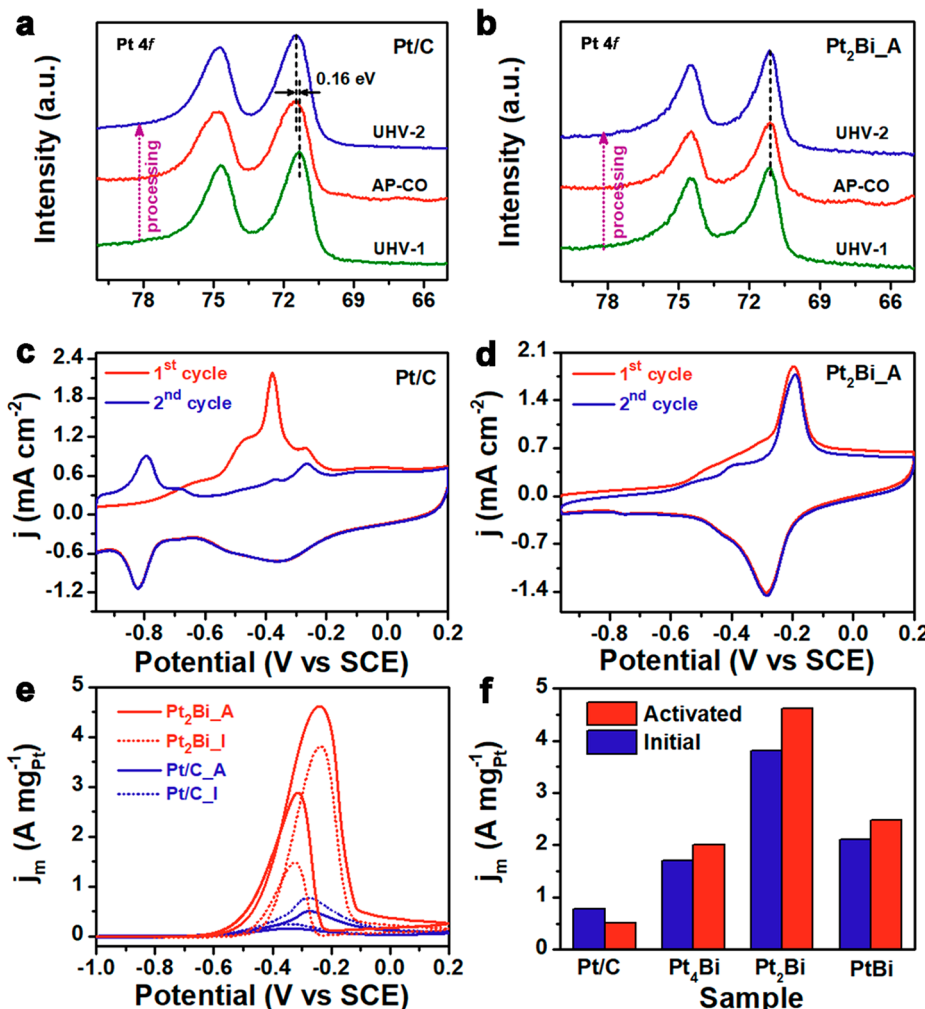


**Figure 4.** AP-XPS spectra of (a) Pt/C and (b) Pt<sub>2</sub>Bi\_A at Pt 4f orbitals under three successive atmospheric conditions. (1) Ultrahigh vacuum (UHV-1, olive line); (2) CO atmosphere (AP-CO, red line); and (3) ultrahigh vacuum (UHV-2, blue line). The incipient X-ray energy is 560 eV. CO-stripping experiment of (c) Pt/C and (d) Pt<sub>2</sub>Bi\_A in 1 M KOH. Scanning rate is 50 mV s<sup>-1</sup>. (e) CV curves of Pt/C and Pt<sub>2</sub>Bi in 1 M KOH/1 M methanol before and after electrochemical treatment. Scanning rate is 50 mV s<sup>-1</sup>. (f) Mass activities of Pt/C, Pt<sub>4</sub>Bi, Pt<sub>2</sub>Bi, and PtBi toward MOR.

was carried out to study the coordination environment of Pt<sub>2</sub>Bi catalysts before and after electrochemical treatment (Figure 3c). The peak position in  $R$  space is related to the atomic distance between surrounding atoms and the absorber, while the peak intensity is proportional to the coordination number of the corresponding surrounding atoms around the absorbing atom. Pt-metal (Pt-M) scattering paths contribute to the features around 2.6 Å. For Pt<sub>2</sub>Bi catalysts, Pt-M consists of two single scattering paths, Pt–Pt at shorter radial distance and Pt–Bi at slightly longer radial distance, which almost overlap with each other. The electrochemical treatment results in the Pt-M peak shifting to a shorter radial distance, which is presumably because of the increase of coordinated Pt and decrease of coordinated Bi around central Pt atoms as a result of structural evolution. Generally, fitting EXAFS in  $R$  space or  $k$  space is used to identify the local structure of the central atoms. Often an atom shell, i.e., of all the neighboring atoms at a specific distance, consists of only one type of atom. If such a shell comprises atoms of different elements, however, their waves cannot be separated by the Fourier transform approach. For example, due to the very close radial distance of Pt and Bi, Pt–Pt and Pt–Bi signals cannot be well separated by Fourier

transform of EXAFS of Pt<sub>2</sub>Bi before and after electrochemical treatment. Wavelet transform (WT) resolves the centers of the backscattering wave functions in energy (or  $k$ ) space and, therefore, offers a straightforward way to discriminate different atoms within one atomic shell.<sup>49</sup> The WT contour plots show two intensity maxima at  $R = 2.58$  Å,  $k = 12.6$  Å<sup>-1</sup> and  $R = 2.63$  Å,  $k = 9$  Å<sup>-1</sup>, assigned to the Pt–Pt scattering path and Pt–Bi scattering path, respectively (Figure 3d). The intensity maximum at the Bi dominating zone becomes weaker and the Pt dominating zone shows an obvious enhancement, demonstrating that the coordination environment varies from coexistence of Pt–Pt and Pt–Bi bonds to a Pt–Pt bond dominating situation after electrochemical treatment. The same trend is also observed in Pt<sub>4</sub>Bi and PtBi samples (Figure S9). The XANES spectra of Pt<sub>2</sub>Bi\_I and Pt<sub>2</sub>Bi\_A at the Bi L<sub>2,3</sub>-edge show similar features with the Bi<sub>2</sub>O<sub>3</sub> spectrum but with a broadened whiteline peak (Figure 3e). The linear combination fitting toward spectra were conducted using Bi foil and Bi<sub>2</sub>O<sub>3</sub> as references (Figure S10). The amount of Bi<sup>0</sup> species decreases significantly after electrochemical treatment which is consistent with XPS results.

Moreover, the absence of peaks from hydrogen under-potential deposition in the range of  $-0.9$  V to  $-0.6$  V (Figure S11) further suggests the coverage of  $\text{Bi}^{3+}$  species on the Pt surface. With the help of XPS, XANES and EXAFS analyses, we now get a comprehensive understanding of the structural evolution of PtBi catalysts. After the electrochemical reconstruction, Bi species partially leach out from  $\text{Pt}_2\text{Bi}_\text{I}$ , generating a unique  $\text{BiO}_x(\text{OH})_y\text{-Pt}$  inverse interface, and results in Pt with an electron-deficient state.

To substantiate its enhanced antipoisoning ability toward CO adsorbate, ambient pressure X-ray photoelectron spectroscopy (AP-XPS) was conducted. Commercial Pt/C and  $\text{Pt}_2\text{Bi}_\text{A}$  were subjected to three successive atmospheric conditions, changing from ultrahigh vacuum (UHV-1,  $3 \times 10^{-8}$  bar) to near ambient pressure (AP-CO,  $5 \times 10^{-4}$  bar, CO atmosphere) and then back to ultrahigh vacuum (UHV-2,  $3 \times 10^{-8}$  bar). In the case of Pt/C (Figure 4a), two peaks located at 71.30 and 74.65 eV are ascribed to  $\text{Pt } 4f_{7/2}$  and  $4f_{5/2}$  orbitals, respectively, with a clean surface (olive line). Subsequently switching to CO atmosphere induces an obvious peak shift of 0.16 eV toward higher binding energy (red line), and the peak shift keeps constant even after pumping back to initial ultrahigh vacuum (blue line). The peak shift is triggered by adsorbed CO on Pt sites by a forming chemical bond,<sup>50</sup> revealing its intrinsic nature of being poisoned. However, no peak shift is observed at Pt 4f orbitals (Figure 4b) and Bi 4f orbitals (Figure S12) in the case of  $\text{Pt}_2\text{Bi}_\text{A}$ , indicating an impressive CO tolerance capacity compared to Pt/C. Additionally, the CO-stripping experiment provides solid evidence for weakened CO adsorption in electrolyte (Figure 4c and d). For Pt/C, two oxidation peaks are observed in the forward scan over a range of  $-0.5$  V to  $-0.3$  V, ascribed to CO oxidative removal on Pt.<sup>25</sup> Impressively, CV curves for  $\text{Pt}_2\text{Bi}_\text{A}$  in the first scan and second scan almost overlap, indicating that CO molecules are barely adsorbed on  $\text{Pt}_2\text{Bi}_\text{A}$ . The enhanced CO tolerance is expected to derive from the electron-deficient state of Pt, which efficiently weakens the CO adsorption. In addition, the removal of CO adsorbates can also be facilitated by rich OH species from another Pt site or  $\text{BiO}_x(\text{OH})_y$  based on bifunctional mechanism.<sup>6,25</sup>

To experimentally confirm the enhancement of the  $\text{BiO}_x(\text{OH})_y\text{-Pt}$  inverse interface structure on the catalytic performance of PtBi catalysts, the MOR activities of  $\text{Pt}_2\text{Bi}$  and commercial 20 wt % Pt/C catalysts were evaluated in a typical three-electrode system using electrolyte containing 1 M KOH and 1 M methanol. CV curves of  $\text{Pt}_2\text{Bi}$  and Pt/C before and after electrochemical treatment are shown in Figure 4e. Peaks that appear at a high voltage in a forward scan are ascribed to methanol oxidation, while the peaks at a low voltage in a backward scan are assigned to the oxidation of intermediates.<sup>25</sup> Peak current density normalized by loading mass of Pt in the forward scan is used to estimate activities of catalysts. For  $\text{Pt}_2\text{Bi}$  catalyst, the mass activity increases from 3806 to 4611 mA  $\text{mg}^{-1}\text{pt}$  after electrochemical treatment. However, in the case of commercial Pt/C, the mass activity decreases from 774 to 504 mA  $\text{mg}^{-1}\text{pt}$ . To verify the activity enhancement induced by electrochemical treatment, PtBi nanoparticles with different compositions were synthesized through simply adjusting the feeding molar ratios of Pt and Bi precursors (Figure S13). The feeding ratio has a great influence on the morphology of the nanoparticles. High Pt content prefers the growth of chain-like structures, while a high Bi content prefers the formation of plate-like structures. It should be noticed that the fcc-Pt phase

is dominating in all samples based on XRD patterns (Figure S14). The activation phenomenon is universal for all PtBi catalysts and activation time is dependent on the Pt/Bi ratios, in which longer treatment time is required for higher Bi content. The moment when the highest catalytic activity is reached is used as the criterion for the complete electrochemical reconstruction. As shown in Figure 4f, specific mass activities of  $\text{Pt}_4\text{Bi}$ ,  $\text{Pt}_2\text{Bi}$ , and PtBi are  $2000 \text{ mA mg}^{-1}\text{pt}$ ,  $4611 \text{ mA mg}^{-1}\text{pt}$ , and  $2480 \text{ mA mg}^{-1}\text{pt}$ , which are 1.17, 1.21, and 1.18 times that of their initial states ( $1713 \text{ mA mg}^{-1}\text{pt}$ ,  $3806 \text{ mA mg}^{-1}\text{pt}$ , and  $2110 \text{ mA mg}^{-1}\text{pt}$ ), respectively. In the case of commercial Pt/C, the activity decays after a similar treatment (1 h). The electrochemical treatment is critical for enhancing the catalytic activity of PtBi catalysts.  $\text{Pt}_2\text{Bi}$  manifests the highest activity among all samples, which is 2.31, 1.86, and 5.96 times higher than that of  $\text{Pt}_4\text{Bi}$ , PtBi, and pristine commercial Pt/C, respectively. In addition, the catalytic durability and recyclability of different catalysts were evaluated in a solution containing 1 M KOH and 1 M methanol by using a chronoamperometric measurement at  $-0.23$  V (Figures S15 and S16).  $\text{Pt}_2\text{Bi}_\text{A}$  shows an excellent durability as evidenced by the fact that a mass activity of  $1520 \text{ mA mg}^{-1}\text{pt}$  can be maintained even after a continuous test for 10000 s, which is much higher than that of Pt/C ( $278 \text{ mA mg}^{-1}\text{pt}$ ). The high activity and great durability of  $\text{Pt}_2\text{Bi}_\text{A}$  make it among one of the best MOR electrocatalysts reported so far (Table S3). Therefore, the existence of the  $\text{BiO}_x(\text{OH})_y\text{-Pt}$  inverse interface can dramatically improve the catalytic performance toward MOR.

## CONCLUSION

In conclusion, we have demonstrated the formation of the  $\text{BiO}_x(\text{OH})_y\text{-Pt}$  inverse interface through electrochemical reconstruction. By combining DFT calculations, XAS, AP-XPS and electrochemical characterizations, we revealed that the incorporation of  $\text{BiO}_x(\text{OH})_y$  could tailor the electronic structure and local coordination environment of Pt, resulting in weakened CO and strengthened OH at Pt sites. Moreover, it is worth noting that  $\text{BiO}_x(\text{OH})_y$  also can provide rich OH species for oxidative removal of adsorbed CO. The synergy between the electronic effect and bifunctional effect strengthens the resistance to poisonous CO species. In virtue of the  $\text{BiO}_x(\text{OH})_y\text{-Pt}$  inverse interface, the optimal  $\text{Pt}_2\text{Bi}$  sample manifests a mass activity of  $4611 \text{ mA mg}^{-1}\text{pt}$ , which is 5.96 times higher than that of commercial Pt/C and shows an excellent durability as retained at  $1520 \text{ mA mg}^{-1}\text{pt}$  after a chronoamperometric test for 10000 s. This work emphasizes the rational engineering of the interfaces in the composite electrocatalysts and provides deeper insight into the structure–property relationship, offering great opportunities for fabrication of high-performance electrocatalysts for green energy technologies.

## ASSOCIATED CONTENT

### Supporting Information

The Supporting Information is available free of charge at <https://pubs.acs.org/doi/10.1021/acs.nanolett.0c03340>.

Experimental procedures, characterizations, Figures S1–S16, and Tables S1–S3 (PDF)

## AUTHOR INFORMATION

### Corresponding Authors

Fenglei Lyu – Institute of Functional Nano & Soft Materials (FUNSOM), Jiangsu Key Laboratory for Carbon-Based Functional Materials and Devices, Soochow University, Suzhou 215123, Jiangsu, China;  [orcid.org/0000-0002-9019-1909](https://orcid.org/0000-0002-9019-1909); Email: [flv@suda.edu.cn](mailto:flv@suda.edu.cn)

Tao Cheng – Institute of Functional Nano & Soft Materials (FUNSOM), Jiangsu Key Laboratory for Carbon-Based Functional Materials and Devices, Soochow University, Suzhou 215123, Jiangsu, China;  [orcid.org/0000-0003-4830-177X](https://orcid.org/0000-0003-4830-177X); Email: [tcheng@suda.edu.cn](mailto:tcheng@suda.edu.cn)

Tsun-Kong Sham – Department of Chemistry, University of Western Ontario, London, Ontario N6A5B7, Canada;  [orcid.org/0000-0003-1928-6697](https://orcid.org/0000-0003-1928-6697); Email: [tsham@uwo.ca](mailto:tsham@uwo.ca)

Qiao Zhang – Institute of Functional Nano & Soft Materials (FUNSOM), Jiangsu Key Laboratory for Carbon-Based Functional Materials and Devices, Soochow University, Suzhou 215123, Jiangsu, China;  [orcid.org/0000-0001-9682-3295](https://orcid.org/0000-0001-9682-3295); Email: [qiaozhang@suda.edu.cn](mailto:qiaozhang@suda.edu.cn)

### Authors

Xuchun Wang – Institute of Functional Nano & Soft Materials (FUNSOM), Jiangsu Key Laboratory for Carbon-Based Functional Materials and Devices, Soochow University, Suzhou 215123, Jiangsu, China; Department of Chemistry, University of Western Ontario, London, Ontario N6A5B7, Canada

Miao Xie – Institute of Functional Nano & Soft Materials (FUNSOM), Jiangsu Key Laboratory for Carbon-Based Functional Materials and Devices, Soochow University, Suzhou 215123, Jiangsu, China;  [orcid.org/0000-0002-9797-1449](https://orcid.org/0000-0002-9797-1449)

Yun-Mui Yiu – Department of Chemistry, University of Western Ontario, London, Ontario N6A5B7, Canada

Zhiqiang Wang – Department of Chemistry, University of Western Ontario, London, Ontario N6A5B7, Canada;  [orcid.org/0000-0003-0628-5222](https://orcid.org/0000-0003-0628-5222)

Jiatang Chen – Department of Chemistry, University of Western Ontario, London, Ontario N6A5B7, Canada;  [orcid.org/0000-0002-9705-6523](https://orcid.org/0000-0002-9705-6523)

Lo-Yueh Chang – Institute of Functional Nano & Soft Materials (FUNSOM), Jiangsu Key Laboratory for Carbon-Based Functional Materials and Devices, Soochow University, Suzhou 215123, Jiangsu, China

Yujian Xia – Institute of Functional Nano & Soft Materials (FUNSOM), Jiangsu Key Laboratory for Carbon-Based Functional Materials and Devices, Soochow University, Suzhou 215123, Jiangsu, China

Qixuan Zhong – Institute of Functional Nano & Soft Materials (FUNSOM), Jiangsu Key Laboratory for Carbon-Based Functional Materials and Devices, Soochow University, Suzhou 215123, Jiangsu, China

Mingyu Chu – Institute of Functional Nano & Soft Materials (FUNSOM), Jiangsu Key Laboratory for Carbon-Based Functional Materials and Devices, Soochow University, Suzhou 215123, Jiangsu, China

Hao Yang – Institute of Functional Nano & Soft Materials (FUNSOM), Jiangsu Key Laboratory for Carbon-Based Functional Materials and Devices, Soochow University, Suzhou 215123, Jiangsu, China;  [orcid.org/0000-0002-8241-6231](https://orcid.org/0000-0002-8241-6231)

Complete contact information is available at:

<https://pubs.acs.org/10.1021/acs.nanolett.0c03340>

### Author Contributions

<sup>§</sup>The manuscript was written through contributions of all authors. All authors have given approval to the final version of the manuscript. X.W. and M.X. contributed equally to this work.

### Notes

The authors declare no competing financial interest.

## ACKNOWLEDGMENTS

This work is supported by the National Natural Science Foundation of China (21673150, 51922073, 2190030094), the Natural Science Foundation of Jiangsu Province (BK20180097, SBK20190810), the Jiangsu Province High-Level Talents (JNHB-106), and the China Postdoctoral Science Foundation (2019M660128). We acknowledge the financial support from the 111 Project, Collaborative Innovation Center of Suzhou Nano Science and Technology (NANO-CIC), and the Priority Academic Program Development of Jiangsu Higher Education Institutions (PAPD). This research used resources of the Advanced Photon Source (APS), an Office of Science User Facility operated for the U.S. Department of Energy (DOE) Office of Science by Argonne National Laboratory, and was supported by the U.S. DOE under contract no. DEAC02-06CH11357 and by the Canadian Light Source and its funding partners. This research also used resources of the Taiwan Light Source (TLS) and Taiwan Photon Source (TPS) at the National Synchrotron Radiation Research Center (NSRRC), Taiwan, China. The authors would like to thank the beamline scientists Dr. Zou Finfrock at 20BM APS and Dr. Chih-Wen Pao at 44A of Taiwan Photon Source (TPS) for their great help.

## REFERENCES

- (1) Arico, A. S.; Srinivasan, S.; Antonucci, V. DMFCs: from fundamental aspects to technology development. *Fuel Cells* **2001**, *1*, 133–161.
- (2) Zhao, X.; Yin, M.; Ma, L.; Liang, L.; Liu, C.; Liao, J.; Lu, T.; Xing, W. Recent advances in catalysts for direct methanol fuel cells. *Energy Environ. Sci.* **2011**, *4*, 2736–2753.
- (3) Kakati, N.; Maiti, J.; Lee, S. H.; Jee, S. H.; Viswanathan, B.; Yoon, Y. S. Anode catalysts for direct methanol fuel cells in acidic media: do we have any alternative for Pt or Pt–Ru? *Chem. Rev.* **2014**, *114*, 12397–12429.
- (4) Feng, Y.; Liu, H.; Yang, J. A selective electrocatalyst–based direct methanol fuel cell operated at high concentrations of methanol. *Sci. Adv.* **2017**, *3*, No. e1700580.
- (5) Liu, H.; Liu, K.; Zhong, P.; Qi, J.; Bian, J.; Fan, Q.; Ren, K.; Zheng, H.; Han, L.; Yin, Y.; Gao, C. Ultrathin Pt–Ag alloy nanotubes with regular nanopores for enhanced electrocatalytic activity. *Chem. Mater.* **2018**, *30*, 7744–7751.
- (6) Tong, Y.; Yan, X.; Liang, J.; Dou, S. X. Metal-based electrocatalysts for methanol electro-oxidation: progress, opportunities, and challenges. *Small* **2019**, *1904126*.
- (7) Zhang, T.; Sun, Y.; Li, X.; Li, X.; Liu, D.; Liu, G.; Li, C.; Fan, H. J.; Li, Y. PtPdAg hollow nanodendrites: template-free synthesis and high electrocatalytic activity for methanol oxidation reaction. *Small Methods* **2020**, *4*, 1900709.
- (8) Liu, Z.; Qi, J.; Liu, M.; Zhang, S.; Fan, Q.; Liu, H.; Liu, K.; Zheng, H.; Yin, Y.; Gao, C. Aqueous synthesis of ultrathin platinum/non-noble metal alloy nanowires for enhanced hydrogen evolution activity. *Angew. Chem., Int. Ed.* **2018**, *57*, 11678–11682.
- (9) Yang, Y.; Luo, M.; Zhang, W.; Sun, Y.; Chen, X.; Guo, S. Metal surface and interface energy electrocatalysis: fundamentals, performance engineering, and opportunities. *Chem.* **2018**, *4*, 2054–2083.

- (10) Lyu, F.; Cao, M.; Mahsud, A.; Zhang, Q. Interfacial Engineering of Noble Metals for Electrocatalytic Methanol and Ethanol Oxidation. *J. Mater. Chem. A* **2020**, *8*, 15445–15457.
- (11) Feng, Q.; Zhao, S.; He, D.; Tian, S.; Gu, L.; Wen, X.; Chen, C.; Peng, Q.; Wang, D.; Li, Y. Strain engineering to enhance the electrooxidation performance of atomic-layer Pt on intermetallic Pt<sub>3</sub>Ga. *J. Am. Chem. Soc.* **2018**, *140*, 2773–2776.
- (12) Wu, X.; Jiang, Y.; Yan, Y.; Li, X.; Luo, S.; Huang, J.; Li, J.; Shen, R.; Yang, D.; Zhang, H. Tuning surface structure of Pd<sub>3</sub>Pb/Pt<sub>n</sub>Pb nanocrystals for boosting the methanol oxidation reaction. *Adv. Sci.* **2019**, *6*, 1902249.
- (13) Ma, S.-Y.; Li, H.-H.; Hu, B.-C.; Cheng, X.; Fu, Q.-Q.; Yu, S.-H. Synthesis of low Pt-based quaternary PtPdRuTe nanotubes with optimized incorporation of Pd for enhanced electrocatalytic activity. *J. Am. Chem. Soc.* **2017**, *139*, 5890–5895.
- (14) Huang, L.; Zhang, X.; Wang, Q.; Han, Y.; Fang, Y.; Dong, S. Shape-control of Pt–Ru nanocrystals: tuning surface structure for enhanced electrocatalytic methanol oxidation. *J. Am. Chem. Soc.* **2018**, *140*, 1142–1147.
- (15) Zhang, Z.; Luo, Z.; Chen, B.; Wei, C.; Zhao, J.; Chen, J.; Zhang, X.; Lai, Z.; Fan, Z.; Tan, C.; Zhao, M.; Lu, Q.; Li, B.; Zong, Y.; Yan, C.; Wang, G.; Xu, Z. J.; Zhang, H. One-pot synthesis of highly anisotropic five-fold-twinned PtCu nanoframes used as a bifunctional electrocatalyst for oxygen reduction and methanol oxidation. *Adv. Mater.* **2016**, *28*, 8712–8717.
- (16) Li, H.-H.; Fu, Q.-Q.; Xu, L.; Ma, S.-Y.; Zheng, Y.-R.; Liu, X.-J.; Yu, S.-H. Highly crystalline PtCu nanotubes with three dimensional molecular accessible and restructured surface for efficient catalysis. *Energy Environ. Sci.* **2017**, *10*, 1751–1756.
- (17) Huang, J.; Liu, Y.; Xu, M.; Wan, C.; Liu, H.; Li, M.; Huang, Z.; Duan, X.; Pan, X.; Huang, Y. PtCuNi tetrahedra catalysts with tailored surfaces for efficient alcohol oxidation. *Nano Lett.* **2019**, *19*, 5431–5436.
- (18) Zhang, W.; Yang, Y.; Huang, B.; Lv, F.; Wang, K.; Li, N.; Luo, M.; Chao, Y.; Li, Y.; Sun, Y.; Xu, Z.; Qin, Y.; Yang, W.; Zhou, J.; Du, Y.; Su, D.; Guo, S. Ultrathin PtNiM (M = Rh, Os, and Ir) nanowires as efficient fuel oxidation electrocatalytic materials. *Adv. Mater.* **2019**, *31*, 1805833.
- (19) Li, M.; Duanmu, K.; Wan, C.; Cheng, T.; Zhang, L.; Dai, S.; Chen, W.; Zhao, Z.; Li, P.; Fei, H.; Zhu, Y.; Yu, R.; Luo, J.; Zang, K.; Lin, Z.; Ding, M.; Huang, J.; Sun, H.; Guo, J.; Pan, X.; Goddard, W. A.; Sautet, P.; Huang, Y.; Duan, X. Single-atom tailoring of platinum nanocatalysts for high-performance multifunctional electrocatalysis. *Nat. Catal.* **2019**, *2*, 495–503.
- (20) Lu, S.; Li, H.; Sun, J.; Zhuang, Z. Promoting the methanol oxidation catalytic activity by introducing surface nickel on platinum nanoparticles. *Nano Res.* **2018**, *11*, 2058–2068.
- (21) Yang, P.; Yuan, X.; Hu, H.; Liu, Y.; Zheng, H.; Yang, D.; Chen, L.; Cao, M.; Xu, Y.; Min, Y.; Li, Y.; Zhang, Q. Solvothermal synthesis of alloyed PtNi colloidal nanocrystal clusters (CNCs) with enhanced catalytic activity for methanol oxidation. *Adv. Funct. Mater.* **2018**, *28*, 1704774.
- (22) Xia, B. Y.; Wu, H. B.; Li, N.; Yan, Y.; Lou, X. W.; Wang, X. One-pot synthesis of Pt–Co alloy nanowire assemblies with tunable composition and enhanced electrocatalytic properties. *Angew. Chem., Int. Ed.* **2015**, *54*, 3797–3801.
- (23) Tao, L.; Shi, Y.; Huang, Y.-C.; Chen, R.; Zhang, Y.; Huo, J.; Zou, Y.; Yu, G.; Luo, J.; Dong, C.-L.; Wang, S. Interface engineering of Pt and CeO<sub>2</sub> nanorods with unique interaction for methanol oxidation. *Nano Energy* **2018**, *53*, 604–612.
- (24) Dao, D. V.; Adilbush, G.; Le, T. D.; Nguyen, T. T.D.; Lee, I.-H.; Yu, Y.-T. Au@CeO<sub>2</sub> nanoparticles supported Pt/C electrocatalyst to improve the removal of CO in methanol oxidation reaction. *J. Catal.* **2019**, *377*, 589–599.
- (25) Huang, W.; Wang, H.; Zhou, J.; Wang, J.; Duchesne, P. N.; Muir, D.; Zhang, P.; Han, N.; Zhao, F.; Zeng, M.; Zhong, J.; Jin, C.; Li, Y.; Lee, S.-T.; Dai, H. Highly active and durable methanol oxidation electrocatalyst based on the synergy of platinum–nickel hydroxide–graphene. *Nano Commun.* **2015**, *6*, 10035.
- (26) Cao, L.; Liu, W.; Luo, Q.; Yin, R.; Wang, B.; Weissenrieder, J.; Soldemo, M.; Yan, H.; Lin, Y.; Sun, Z.; Ma, C.; Zhang, W.; Chen, S.; Wang, H.; Guan, Q.; Yao, T.; Wei, S.; Yang, J.; Lu, J. Atomically dispersed iron hydroxide anchored on Pt for preferential oxidation of CO in H<sub>2</sub>. *Nature* **2019**, *565*, 631–635.
- (27) Chen, Z.; Liu, Y.; Liu, C.; Zhang, J.; Chen, Y.; Hu, W.; Deng, Y. Engineering the metal/oxide interface of Pd nanowire@CuO<sub>x</sub> electrocatalysts for efficient alcohol oxidation reaction. *Small* **2020**, *16*, 1904964.
- (28) Feng, Y.; Yang, C.; Fang, W.; Huang, B.; Shao, Q.; Huang, X. Anti-poisoned oxygen reduction by the interface modulated Pd@NiO core@shell. *Nano Energy* **2019**, *58*, 234–243.
- (29) Liu, Z.; Huang, E.; Orozco, I.; Liao, W.; Palomino, R. M.; Rui, N.; Duchoň, T.; Nemšák, S.; Grinter, D. C.; Mahapatra, M.; Liu, P.; Rodriguez, J. A.; Senanayake, S. D. Water-promoted interfacial pathways in methane oxidation to methanol on a CeO<sub>2</sub>-Cu<sub>2</sub>O catalyst. *Science* **2020**, *368*, 513–517.
- (30) Rodriguez, J. A.; Ma, S.; Liu, P.; Hrbek, J.; Evans, J.; Pérez, M. Activity of CeO<sub>x</sub> and TiO<sub>x</sub> nanoparticles grown on Au(111) in the water-gas shift reaction. *Science* **2007**, *318*, 1757–1760.
- (31) Yan, H.; Yang, C.; Shao, W.-P.; Cai, L.-H.; Wang, W.-W.; Jin, Z.; Jia, C.-J. Construction of stabilized bulk-nano interfaces for highly promoted inverse CeO<sub>2</sub>/Cu catalyst. *Nat. Commun.* **2019**, *10*, 3470.
- (32) Liao, H.; Wei, C.; Wang, J.; Fisher, A.; Sridharan, T.; Feng, Z.; Xu, Z. J. A multisite strategy for enhancing the hydrogen evolution reaction on a nano-Pd surface in alkaline media. *Adv. Energy Mater.* **2017**, *7*, 1701129.
- (33) Zhao, Z.; Liu, H.; Gao, W.; Xue, W.; Liu, Z.; Huang, J.; Pan, X.; Huang, Y. Surface-engineered PtNi-O nanostructure with record-high performance for electrocatalytic hydrogen evolution reaction. *J. Am. Chem. Soc.* **2018**, *140*, 9046–9050.
- (34) Sun, Y.-N.; Giordano, L.; Goniakowski, J.; Lewandowski, M.; Qin, Z.-H.; Noguera, C.; Shaikhutdinov, S.; Pacchioni, G.; Freund, H.-J. The interplay between structure and CO oxidation catalysis on metal-supported ultrathin oxide films. *Angew. Chem., Int. Ed.* **2010**, *49*, 4418–4421.
- (35) Yang, F.; Graciani, J.; Evans, J.; Liu, P.; Hrbek, J.; Sanz, J. F.; Rodriguez, J. A. CO oxidation on inverse CeO<sub>x</sub>/Cu(111) catalysts: high catalytic activity and ceria-promoted dissociation of O<sub>2</sub>. *J. Am. Chem. Soc.* **2011**, *133*, 3444–3451.
- (36) Jiang, H.; He, Q.; Zhang, Y.; Song, L. Structural self-reconstruction of catalysts in electrocatalysis. *Acc. Chem. Res.* **2018**, *51*, 2968–2977.
- (37) Jin, S. Are metal chalcogenides, nitrides, and phosphides oxygen evolution catalysts or bifunctional catalysts? *ACS Energy Lett.* **2017**, *2*, 1937–1938.
- (38) Zheng, X.; Zhang, B.; De Luna, P.; Liang, Y.; Comin, R.; Voznyy, O.; Han, L.; García de Arquer, F. P.; Liu, M.; Dinh, C. T.; Regier, T.; Dynes, J. J.; He, S.; Xin, H. L.; Peng, H.; Prendergast, D.; Du, X.; Sargent, E. H. Theory-driven design of high-valence metal sites for water oxidation confirmed using *in situ* soft X-ray absorption. *Nat. Chem.* **2018**, *10*, 149–154.
- (39) Strasser, P.; Koh, S.; Anniyev, T.; Greeley, J.; More, K.; Yu, C.; Liu, Z.; Kaya, S.; Nordlund, D.; Ogasawara, H.; Toney, M. F.; Nilsson, A. Lattice-strain control of the activity in dealloyed core-shell fuel cell catalysts. *Nat. Chem.* **2010**, *2*, 454–460.
- (40) Zhang, B.-W.; Lai, W.-H.; Sheng, T.; Qu, X.-M.; Wang, Y.-X.; Ren, L.; Zhang, L.; Du, Y.; Jiang, Y.-X.; Sun, S.-G.; Dou, S.-X. Ordered platinum–bismuth intermetallic clusters with Pt-skin for a highly efficient electrochemical ethanol oxidation reaction. *J. Mater. Chem. A* **2019**, *7*, 5214–5220.
- (41) Qin, Y.; Luo, M.; Sun, Y.; Li, C.; Huang, B.; Yang, Y.; Li, Y.; Wang, L.; Guo, S. Intermetallic *hcp*-PtBi/*fcc*-Pt core/shell nanoplates enable efficient bifunctional oxygen reduction and methanol oxidation electrocatalysis. *ACS Catal.* **2018**, *8*, 5581–5590.
- (42) Feng, Y.; Shao, Q.; Lv, F.; Bu, L.; Guo, J.; Guo, S.; Huang, X. Intermetallic PtBi nanoplates boost oxygen reduction catalysis with superior tolerance over chemical fuels. *Adv. Sci.* **2020**, *7*, 1800178.

- (43) Yuan, X.; Jiang, X.; Cao, M.; Chen, L.; Nie, K.; Zhang, Y.; Xu, Y.; Sun, X.; Li, Y.; Zhang, Q. Intermetallic PtBi core/ultrathin Pt shell nanoplates for efficient and stable methanol and ethanol electro-oxidation. *Nano Res.* **2019**, *12*, 429–436.
- (44) Yuan, X.; Zhang, Y.; Cao, M.; Zhou, T.; Jiang, X.; Chen, J.; Lyu, F.; Xu, Y.; Luo, J.; Zhang, Q.; Yin, Y. Bi(OH)<sub>3</sub>/PdBi composite nanochains as highly active and durable electrocatalysts for ethanol oxidation. *Nano Lett.* **2019**, *19*, 4752–4759.
- (45) Yang, M. Catalytic activities of PtBi nanoparticles toward methanol electrooxidation in acid and alkaline media. *J. Power Sources* **2013**, *229*, 42–47.
- (46) Ferrin, P.; Mavrikakis, M. Structure sensitivity of methanol electrooxidation on transition metals. *J. Am. Chem. Soc.* **2009**, *131*, 14381–14389.
- (47) Blyholder, G. Molecular orbital view of chemisorbed carbon monoxide. *J. Phys. Chem.* **1964**, *68*, 2772–2777.
- (48) Zu, M. Y.; Zhang, L.; Wang, C.; Zheng, L. R.; Yang, H. G. Copper-modulated bismuth nanocrystals alter the formate formation pathway to achieve highly selective CO<sub>2</sub> electroreduction. *J. Mater. Chem. A* **2018**, *6*, 16804–16809.
- (49) Muñoz, M.; Argoul, P.; Farges, F. Continuous Cauchy wavelet transform analyses of EXAFS spectra: A qualitative approach. *Am. Mineral.* **2003**, *88*, 694–700.
- (50) Tao, F.; Dag, S.; Wang, L.-W.; Liu, Z.; Butcher, D. R.; Bluhm, H.; Salmeron, M.; Somorjai, G. A. Break-up of stepped platinum catalyst surfaces by high CO coverage. *Science* **2010**, *327*, 850.